Atmos. Chem. Phys., 12, 1701–1720, 2012
www.atmos-chem-phys.net/12/1701/2012/
doi:10.5194/acp-12-1701-2012

Atmospheric Chemistry and Physics

Gravity wave variances and propagation derived from AIRS radiances

J. Gong[1], **D. L. Wu**[1,*], **and S. D. Eckermann**[2]

[1]Jet Propulsion Laboratory, California Institute of Technology, Pasadena, CA 91109, USA
[2]Naval Research Laboratory, Washington DC 20375, USA
[*]now at: Goddard Space Flight Center, Greenbelt, MD 20771, USA

Correspondence to: J. Gong (jie.gong@jpl.nasa.gov)

Received: 17 November 2010 – Published in Atmos. Chem. Phys. Discuss.: 15 April 2011
Revised: 31 January 2012 – Accepted: 4 February 2012 – Published: 16 February 2012

Abstract. As the first gravity wave (GW) climatology study using nadir-viewing infrared sounders, 50 Atmospheric Infrared Sounder (AIRS) radiance channels are selected to estimate GW variances at pressure levels between 2–100 hPa. The GW variance for each scan in the cross-track direction is derived from radiance perturbations in the scan, independently of adjacent scans along the orbit. Since the scanning swaths are perpendicular to the satellite orbits, which are inclined meridionally at most latitudes, the zonal component of GW propagation can be inferred by differencing the variances derived between the westmost and the eastmost viewing angles.

Consistent with previous GW studies using various satellite instruments, monthly mean AIRS variance shows large enhancements over meridionally oriented mountain ranges as well as some islands at winter hemisphere high latitudes. Enhanced wave activities are also found above tropical deep convective regions. GWs prefer to propagate westward above mountain ranges, and eastward above deep convection. AIRS 90 field-of-views (FOVs), ranging from +48° to −48° off nadir, can detect large-amplitude GWs with a phase velocity propagating preferentially at steep angles (e.g., those from orographic and convective sources). The annual cycle dominates the GW variances and the preferred propagation directions for all latitudes. Indication of a weak two-year variation in the tropics is found, which is presumably related to the Quasi-biennial oscillation (QBO).

AIRS geometry makes its out-tracks capable of detecting GWs with vertical wavelengths substantially shorter than the thickness of instrument weighting functions. The novel discovery of AIRS capability of observing shallow inertia GWs will expand the potential of satellite GW remote sensing and provide further constraints on the GW drag parameterization schemes in the general circulation models (GCMs).

1 Introduction

Gravity waves (GWs) are known to play a key role in global climate and weather dynamics by transporting energy and momentum from the lower to the upper atmosphere, transport which is essential for determining the general circulation and temperature structure in the stratosphere and mesosphere (e.g., mesosphere wind reversal, quasi-biennial oscillation, etc.). GWs are of particular importance for wave dynamics in the summer hemisphere in the stratosphere where planetary waves are weak, and are important in the entire mesosphere. As an example, model simulation results suggest that the mesosphere summer easterlies would arrive one month late without including gravity wave drag (GWD) in the model (Scaife et al., 2002). GWs also affect weather and chemistry. For example, temperature fluctuations associated with GWs can lead to formation of polar stratospheric clouds (PSCs) in a synoptically warm condition and susequently affect ozone depletion (Hamill and Toon, 1991).

The importance of gravity waves on climate and weather became widely recognized in recent decades due to progress in observational techniques and model improvements. Two issues remain as major concerns, however. Firstly, a significant amount of the GWs cannot be resolved in GCMs and hence need to be parameterized except those with long wavelengths and low frequencies. These prescribed parameters,

formulated to be dependent on detailed characteristics of GWs and GW sources, however, are poorly constrained by observations, and are actually heavily "tuned" in most of the cases to attain a realistic atmosphere. For example, one of the major GW sources, convection, is often assumed to be uniformly distributed all over the globe in GCMs with spectral GWD parameterization schemes, which is obviously far from reality (Alexander and Rosenlof, 2003). The other important non-stationary GW source – jet imbalances – is not included in most of the GCMs (Kim et al., 2003). Secondly, different observational instruments can only see partial gravity wave spectra. Although solving this jigsaw puzzle is underway (e.g., Alexander et al., 2010), the high-frequency portion of the spectrum is invisible to most of the instruments (Wu et al., 2006; Alexander et al., 2010), and the momentum flux associated with these waves remain uncertain. GWs of higher intrinsic frequency and shorter horizontal wavelengths can potentially carry greater momentum flux than lower frequency GWs, and could therefore exert significant wave drag (Fritts and Alexander, 2003). Currently we are missing global information in particular on these shorter horizontal scale waves. This presents an important information gap for any effort to constrain gravity wave drag (GWD) in climate models by measurements.

Among various GW observations, satellite instruments have advantages over others (e.g., radiosonde, radar, aircraft measurements) in terms of high and regular sampling density and global coverage. As an example, the Aqua satellite, which carries the Atmospheric Infrared Sounder (AIRS), samples each $2^\circ \times 2^\circ$ latitude-longitude gridbox at least 24 times per month. Intercomparisons and cross-validations can therefore be readily carried out among different satellite instruments on a global basis. Based on their viewing geometry, satellite GW observational instruments can be further categorized into three groups: limb, sub-limb, and nadir sounders. The limb sounders (e.g., LIMS, CRISTA, HIRDLS, GPS) are sensitive to GWs with λ_z/λ_h ratio of less than 1/10–1/20, i.e., low-frequency GWs. Here λ_z and λ_x denote vertical and horizontal wavelength, respectively. The nadir sounders (e.g., AIRS, AMSU-A, SSMIS) are most sensitive to high-frequency GWs, and the sub-limb sounders (e.g., MLS) are sensitive to mid-frequency GWs. Table A1 summarizes the sensitivities of wave parameters from four satellite instruments that are compared with AIRS results later on. More details can be found in Wu et al. (2006) and Preusse et al. (2009).

As a nadir viewing sounder, AIRS has at least three supurb properties for GW studies. Firstly, AIRS has a high horizontal resolution ($\sim$13 km at nadir). Therefore AIRS is very sensitive to high-frequency GWs, which are badly constrained in their global distributions by both observations and models. Secondly, for the outer tracks the sensitivity depends on the tilt of the wave fronts. This allows us to estimate preferential GW propagation directions from the viewing-dependent variance difference between the two outmost off-nadir views. Lastly, AIRS radiances are a direct measure of GW induced air temperature perturbations, and hence provide a more accurate measurement of GWs than retrieved temperatures.

This paper is organized as follows. The following section gives a brief introduction of the AIRS instrument, and a description of the methods we use to retrieve GW properties. In Sect. 3, a climatology of wave variance and the preferred zonal propagation direction will be derived in terms of zonal-mean, geographical distribution and temporal variations. Interpretation of the results is discussed in detail in Sect. 4, where we emphasize on two major gravity wave sources – topography and convection, and their interannual variabilities. Wave enhancements in the equatorial lower stratosphere and the winter pole at 10 hPa will be discussed in a great length, and a numerical experiment is performed to support the speculation on the observed GWs being low-frequency waves. Concluding remarks can be found in Sect. 5.

For reader's convenience, we hereafter refer to "internal GWs" as high-frequency ($\omega \gg f$), long vertical wavelength ($\lambda_z > 10$ km) and short horizontal wavelength waves ($\lambda_h \sim 100$ km or less), and use "inertia GWs" to represent low-frequency ($\omega \sim f$), short vertical wavelength ($\lambda_z < 10$ km) and long horizontal wavelength ($\lambda_h \sim 1000$ km) waves, where ω and f denote wave frequency and the Coriolis parameter. One should keep in mind that GWs in the stratified atmosphere are essentially all internal waves.

2 AIRS instrument and method

AIRS is an infrared spectrometer and sounder that contains 2378 channels in 3.74–4.61 µm, 6.20–8.22 µm and 8.8–15.4 µm wavebands. It makes a cross-track scan every 8/3 second that includes 90 footprints on the ground, 4 independent views over the cold space, and 3 views into 3 different calibrators (Aumann and Miller, 1994). The scan swath is $\sim$1600 km wide, reaching $\pm 48.95^\circ$ from nadir. The angle difference between two adjacent footprints, therefore, is about 1.1°, which corresponds to $\sim$ 13 km footprint size at nadir. The satellite orbits over 24 h are divided into 240 granules, each of which contains 135 scans (6 min duration).

We use AIRS CO_2 15 µm radiance emission bands with wavenumbers ranging from 665 cm^{-1} to 693 cm^{-1} in this study. 50 channels are selected with 11 distinguished weighting functions (WFs) peaking between 2 hPa and 100 hPa. The channel numbers are listed in Table A2 in the Appendix A. Ideally, only channels at the maxima or minima of the radiance spectra, or paired channels at two side-wings of extremes should be used since they are most stable with small detector drifts on the spectra, which mainly occur due to the expansion/contraction of the glass filter depending on whether it faces the Sun or in darkness (i.e., ascending/descending of the orbits). However, we are losing information over most of the middle to upper stratosphere by only selecting these channels. With this consideration, several

channels on one side wing of maxima/minima (bold numbers in Table A2) are also selected. Results from ascending and descending orbits have been compared carefully, and no significant differences have been found whatsoever, so this problem shouldn't cause major problems or failures of using the wing channels in our research.

Since AIRS scans are always perpendicular to the orbit track, the scan line can therefore be treated approximately as along the west-east direction for most of the time, except at high latitudes where the scan is mostly meridional (Aqua satellite orbit track can be checked at http://www.ssec.wisc.edu/datacenter/aqua/). We hence exclude the data beyond $\pm 80^\circ$ latitudes.

The variance of the radiance (σ^2) has three components:

$$\sigma^2 = \sigma^2_{\mathrm{GW}} + \sigma^2_{\mathrm{noise}} + \epsilon^2 \quad (1)$$

Normally other variance (ϵ^2) is much smaller than the first terms on the right-hand of Eq. (1), and hence is omitted here. Evidence shows that AIRS may observe some turbulence signals or small vertical wavelength inertia GWs, which will be discussed later on in Sect. 4.3. However, these additional sources of variance are highly uncertain, and we would rather include them in σ^2_{GW} than separating them out. Since the instrument noise is on the same order with the magnitude of the GWs, it needs to be carefully evaluated and subtracted consequently. The instrument noise ($\sigma^2_{\mathrm{noise}}$) is estimated in an analagous way to Wu and Waters (1996). Instead of using pre-launch information, we feel it is more accurate to estimate the random component of the noise from the real data with the assumption that $\sigma^2_{\mathrm{noise}}$ only depends on the frequency channel, and should not vary with location, time and viewing angle. To extract the radiance noise, we first apply a 3-pt running smooth window to each independent scan and compute the variance as the squared difference between the original and smoothed data (referred as "3-pt result" hereafter). Then, the minimum variance from the monthly averaged $2^\circ \times 2^\circ$ map for each month is determined. Because the 3-pt variance is affected least by GWs, the minimum variance is assumed to be very close to the measurement noise. These minimum variances are found always coming from the summer hemisphere high-latitudes. Finally, the mean is computed for all the variances that are below the median of the timeseries, and we attribute this mean as the instrument noise $\sigma^2_{\mathrm{noise}}$. The 3-pt variance is used for the noise estimation since it gives the smallest cut-off wavelength and hence contains the most high-frequency information. Nevertheless, the 3-pt result still contains a fair amount of GW contributions in that the latitudinal and geographical distributions of the 3-pt result look similar to 7-pt result even without noise subtraction (not shown). The noise estimation method used here is confirmed to be reasonable and accurate by the fact that variance reaches minimum at summer hemisphere high latitudes, and is quite uniformly and stably distributed there throughout the time. Moreover, there are no statistically significant differences among different viewing angles there.

We furthermore compared the noises estimated by the above method with the NEdT (Noise Equivalent Delta Temperature) listed in AIRS property reports (http://airs.jpl.nasa.gov/data_products/algorithms/), and as one can easily tell from Table A2 in the Appendix A, they agree very well. A linear increasing trend has been found in the estimated noise at various levels, which is on the same order of the trend found in the AIRS documentation. Since this trend is far from significant (regression coefficients on the order of $10^{-5}\,\mathrm{K}^2\,\mathrm{month}^{-1}$), which is probably due to the run-off of the sensors, we do not remove the trend in this study.

As suggested by Wu and Waters (1997) and Wu and Eckermann (2008), the minimum detectable GW variance (σ^2_{GW}) is $\sigma^2_{\mathrm{min}} = \sqrt{2(M-2)/N}\,\sigma^2_{\mathrm{noise}}$, where M is the number of points used in this filter for variance estimation ($M = 7$ in this case). Since $\sigma^2_{\mathrm{noise}}$ is determined from a monthly mean $2^\circ \times 2^\circ$ map, a zonal average with N points in this grid size can further reduce the detection threshold. The outmost $M/2$ points are used to get an averaged variance value, which also needs to be considered. The minimum detectable values at various pressure levels are listed in Table A2 in the Appendix A.

We cannot directly calculate the GW horizontal propagation direction from radiance measurements of a single scan. However, the preferred zonal propagation direction can be indirectly inferred from the difference of GW variances between two different FOVs. This is illustrated in a schematic picture Fig. 1, where a typical mountain gravity wave (MW) packet is generated downstream of the mountain under a westerly wind. Wave phases, though stationary in the Earth frame, are propagating downward and westward relative to the westerly mean flow, while energy is propagating upward and westward in this case. In the west field-of-view (FOV) of AIRS, the wave amplitudes are largely smeared out, while the east FOV would yield a much greater reading. Therefore, negative (positive) value of $(\mathrm{GW_w} - \mathrm{GW_e})$ reflects a predominant westward (eastward) zonal propagation. Since multiple factors affect the magnitude of the difference, such as the viewing angle relative to the phase front, the original GW amplitude, etc., the absolute value of the difference does not have a definitive physical meaning. As long as it is statistically significant, the sign of the difference is the variable that really matters. This approach has been formerly used on Aura MLS observations to study GW meridional propagation direction, and has turned to be a very useful and effective method (Wu and Eckermann, 2008).

Before presenting the results, one should note that the majority of the GW signals in AIRS comes from high-frequency GWs. The visibility can be computed as a function of along-track wavelength (λ_x) and vertical wavelength (λ_z) by convolving a plane wave of unity amplitude (1 K) with the weighting function (WF) (McLandress et al., 2000). In the along-track direction, the peak of the sensitivity is mainly determined by the length of the truncation window, as

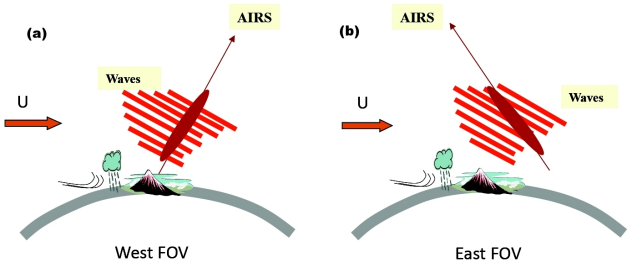

Fig. 1. Cartoons showing the wave smearing effect from different views. **(a)** Westmost off-nadir view, where in this particular case wave signals are largely smeared out; **(b)** Eastmost off-nadir view, where the strongest variance should be observed. Red parallel rectangles represent the phase lines of the GW, while bold red arrows denote the mean wind direction.

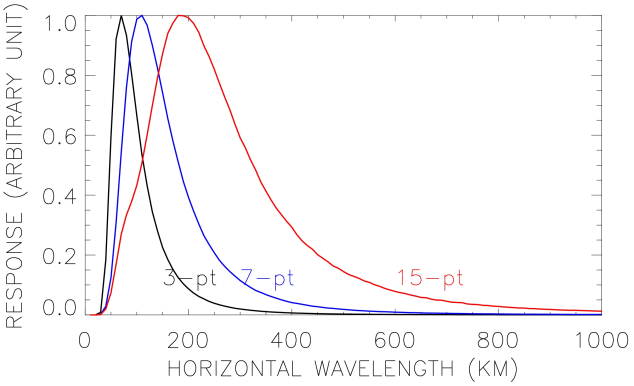

Fig. 2. AIRS visibility as a function of the along-track wavelength with 3-pt (black), 7-pt (blue) and 15-pt (red) running smooth window applied.

suggested by Fig. 2. The left half of the three curves, which is similar for the 3-pt, 7-pt and 15-pt results, is controlled by the width of the AIRS FOV. All three rise sharply once λ_x becomes larger than the footprint size, which is ~ 13 km at nadir. The length of the smoothing window decides the peak as well as the tail of the filter. In the vertical direction, AIRS can hardly detect GWs with λ_z shorter than the full width at half maximum (FWHM) of the WFs, which is ~ 12 km. However, there are some exceptions, which will be discussed later in Sect. 4.3. The sensitivity increases monotonically with the increase of the λ_z before reaching the peak at $\lambda_z \approx \lambda_{x\max}$, where $\lambda_{x\max}$ denotes the most sensitive along-track wavelength. This can be better understood from revisiting Fig. 1, where the largest amplitude would be reached when the GW fronts are parallel to the viewing angle. For a 7-pt window, the peak sensitivity occurs when both λ_x and λ_z equal to ~ 100 km. Alexander and Barnet (2007) studied multiple MW events over the tip of Andes and Antarctic Peninsula, and found out the most dominant λ_x is around 100–150 km. So the 7-pt window can effectively capture these GWs. With a wider window, we are at the cost of possible inclusion of other waves (e.g., Kelvin wave), and we may lose the dominant GWs as suggested by Alexander and Barnet (2007). Nevertheless, the major conclusion's robustness does not depend much on window size. A 3-pt analyses figure is provided in the Appendix B, which shows smaller amplitude and similar patterns to the 7-pt result, implying that 7-pt is a better window to use. We hence only present 7-pt results in this paper.

3 Climatology of gravity wave variances and the preferred zonal propagation direction

The monthly mean latitudinal, geographical and temporal variations will be presented in this section. Year 2005 is used to indicate the mean GW climatology, which represents a condition with no strong sudden stratospheric warming nor ENSO event.

3.1 Latitudinal distributions

Figures 3 and 4 plot the monthly averaged zonal mean 7-pt radiance variance as a function of latitude and height in January and July of 2005, respectively (with estimated instrumental noise deducted), overplotted with UK Met Office monthly mean zonal winds. The variances can be explained by GWs, since they in general grow exponentially with height at mid-high latitudes. In the middle to upper stratosphere (above 20 hPa), the two largest variance centers colocate with the westerly and easterly jet cores in the upper stratosphere, and the one in the winter hemisphere is apparently stronger. This indicates that large amplitude GWs (or frequently generated GWs) are from sources beneath the two jet centers. The overall feature is similar to previous GW studies using Aqua AMSU-A, UARS MLS and Aura MLS (Wu et al., 2006) with comparable strengths in the winter hemisphere, but weaker amplitudes in the summer hemisphere. However, the wave enhancement at the 10 hPa near the winter pole is a new feature revealed by AIRS data. An interpretation of this feature is inertia GWs, which will be discussed in Sect. 4.3. Very low GW activity is observed by AIRS in the summer polar regions. Even without the subtraction of estimated noise, the variance there is still significantly smaller than GW variance derived from other satellite measurements (Wu and Eckermann, 2008). Low phase speed GWs cannot propagate into these regions because of the wind reversal between the troposphere and the stratosphere. In addition, the low wind velocities in the summer high-latitude stratosphere allow AIRS only to observe GWs of high ground-based phase speeds (larger than $\sim 40\,\mathrm{m\,s^{-1}}$; cf. discussion of observational filter by e.g. Alexander, 1998). However, such fast waves should be emitted from sources such as fronts that are currently parameterized in models to

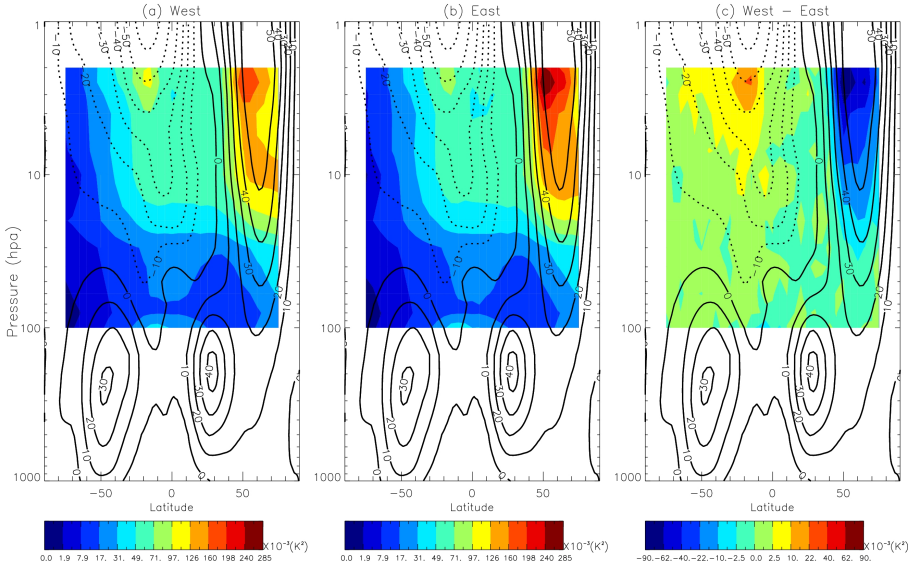

Fig. 3. Zonal mean of the GW variance at the westmost view **(a)**, eastmost view **(b)** and the difference between the westmost and eastmost views **(c)** as a function of latitude and height for January, 2005. Monthly mean zonal winds obtained from UK Met Office are contoured in solid (westerly) and dotted (easterly) lines with an interval of 10 m s^{-1}. The color scale is linear by taking a square-root of the values. In **(c)**, positive (negative) values correspond to preferred eastward (westward) propagation direction.

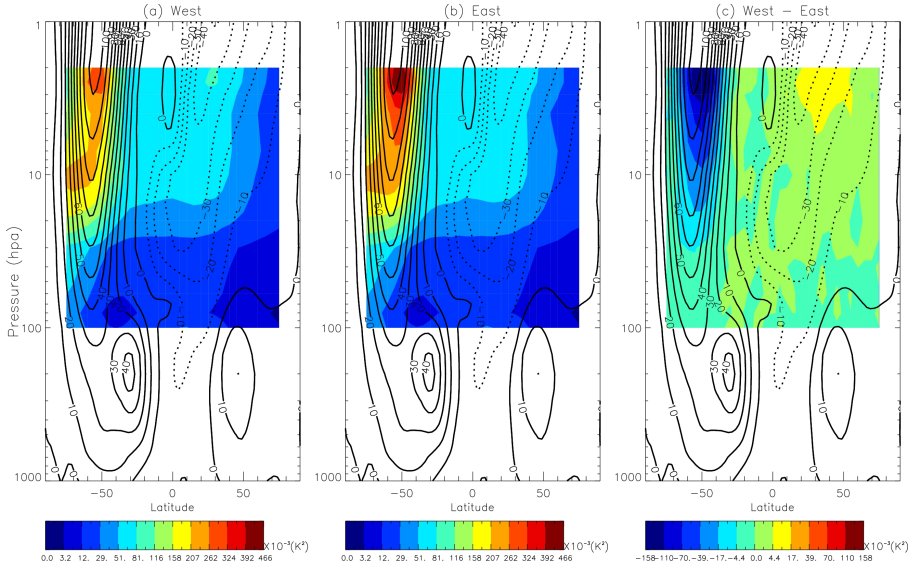

Fig. 4. Same with Fig. 3, except for July 2005.

reproduce the wind reversal around the mesopause (Richter et al., 2010). The very low values in AIRS indicate rather low probability of such waves to occur and support observational evidence that GWs from subtropical convection propagating polewards are a major source of momentum for the high latitude summer mesosphere (Preusse et al., 2009).

In the lower stratosphere, AIRS GW variance is generally larger in the tropics and decreases with latitude. Similar results have been found in some measurements that represent the behavior of the inertia GWs (e.g., Alexander et al., 2002; Wang and Geller, 2003; Ratnam et al., 2004; Preusse et al., 2006) and middle frequency GWs (e.g., Wu and Eckermann, 2008). AMSU-A, which has the same scan angle as AIRS, and hence which is supposed to be also sensitive to internal GWs, observes features opposite to AIRS at the equatorial lower stratosphere where the GW variance reaches minimum (Wu et al., 2006). This interesting feature will be discussed in details later on in Sect. 4.3.

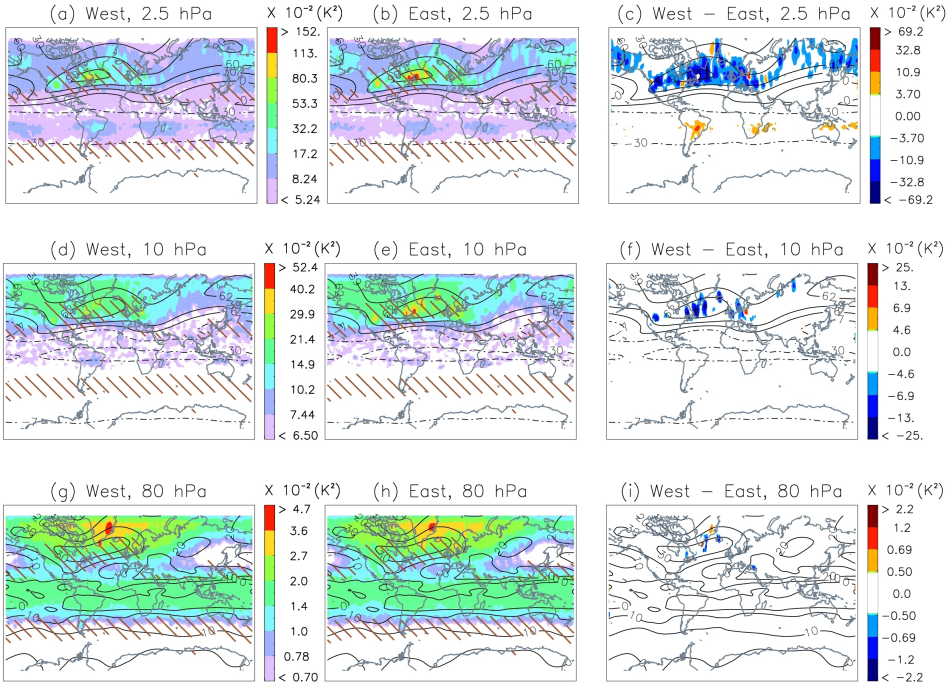

Fig. 5. Geographical distribution of GW variance on a $2^\circ \times 2^\circ$ grid at westmost view (left column), eastmost view (middle column) and the difference (right column) for January 2005 at 2.5, 10, and 80 hPa from top to bottom. 3-pt smoothing has been further applied to make the signals stand out. In the left two columns, values smaller than 2σ are uncolored, where σ is the minimum detectable variance. In the rightmost column, absolute values smaller than the minimum detectable difference are whitened. The UK Met Office monthly mean zonal winds at corresponding levels are contoured in black solid (westward) and dotted (eastward) lines. Total wind velocity greater than $10\,\mathrm{m\,s^{-1}}$ areas at 700 hPa are hatched with brown lines.

As stated in Sect. 2, one can infer the GW preferred zonal propagation direction from the difference of the GW variances between the two outmost views. As in the right columns of Figs. 3 and 4, the zonal mean zonal propagation directions, on a monthly scale, always tend to be in the opposite direction to the mean zonal winds, which is in general westward (eastward) in the winter (summer) hemisphere. This is true especially for large amplitude GWs at high altitudes, as will be shown in the geographical patterns in the next section. Orography is one of the most prominent GW sources in the winter hemisphere. Only in strong westerly winds can mountain waves, which have zero ground- based phase speeds, gain high intrinsic phase-speeds and long vertical wavelengths, and thus become visible to AIRS. Notice that the overall pattern in Fig. 3c does not strictly follow the mean zonal wind contours, as meridional component is missing here.

There is no significant difference between two outmost views at the 10 hPa winter pole and tropical lower stratosphere, which implies the same amount of eastward propagating and westward propagating GWs. Simulation results from Sect. 4.3 confirm this inference.

Very similar features can also be obtained with the 3-pt filter, though the amplitudes are smaller (Appendix B), confirming that the result is robust.

3.2 Geographical distributions

Monthly mean geographical maps are plotted in Figs. 5 and 6 at various levels to represent typical situations of January and July. Only the variance that is larger than $2\sigma_{\min}$ is colored, where $\sigma_{\min}$ is the minimum detectable variance. Zonal mean wind (black solid contours) and wind speed at 700 hPa that exceeds $10\,\mathrm{m\,s^{-1}}$ (brown hatched areas) are overplotted on the variance maps.

Like the zonal mean maps Figs. 3 and 4, GW variances show great enhancements over middle-high latitudes in the winter hemisphere where the polar night jet is the strongest. Clear orographic GW signals can be identified amongst the overall enhancement. In the northern hemisphere (NH), GW variances as well as the differences show great longitudinal dependence. In January 2005, a clear subtropical jet and a mid-latitude jet can be identified from the 700 hPa wind. The mid-latitude jet (which roughly collocates with the upper-level polar night jet) is apparently more powerful in generating the MWs when it encounters big south-north oriented mountain ranges such as Rockies, the tip of the Appalachian mountains (Mts), Greenland, Iceland, and Kjolen Mts at the Scandinavia Peninsula. Since the polar night jet in the stratosphere is also strong and favorably aligned with the troposphere jet over Russia, enhancements can be seen over some

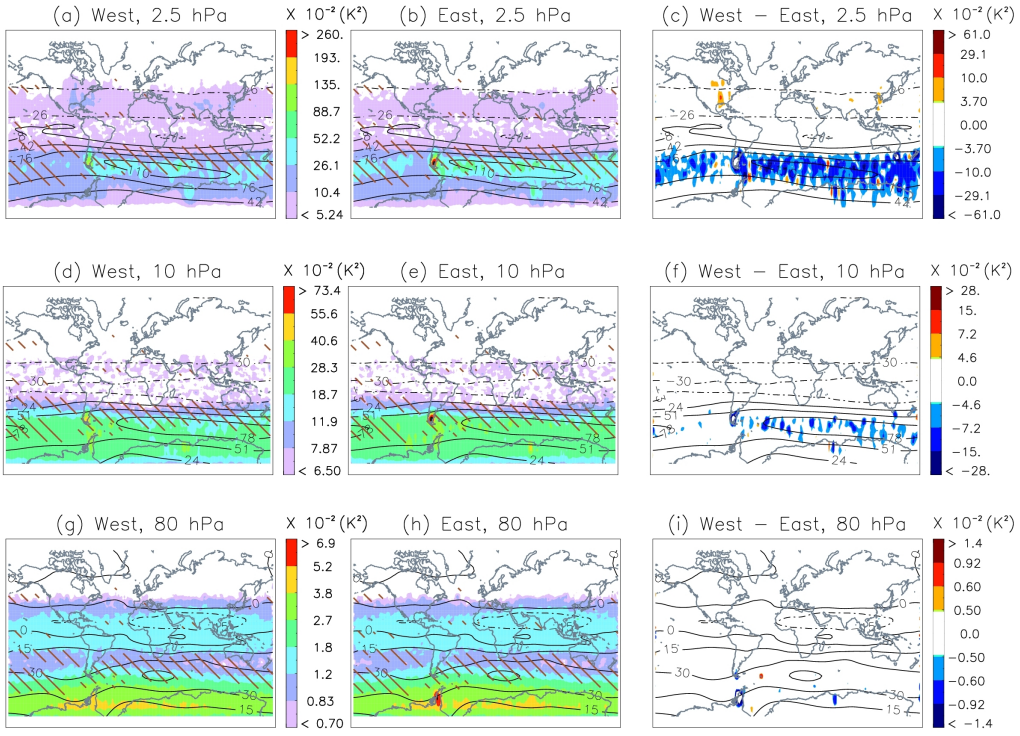

Fig. 6. Same as Fig. 5, except for July 2005.

Russian Mts as well. The subtropical jet, on the contrary, barely generates any large amplitude GWs. That is probably because the subtropical jet center locates in the upper troposphere while the polar jet in the troposphere is closer to the ground, as can be found in Fig. 3. Also, note that wind above the subtropical jet switches direction in the middle to upper stratosphere. One can imagine GWs generated in this region must suffer from critical level filtering or turning point reflection (c.f., Dunkerton, 1984). In the Southern Hemisphere (SH), the two jets in the troposphere are more or less mixed together, and huge MWs are generated over the tip of the Andes, tip of the Antarctic Peninsula, as well as some islands (e.g., New Zealand). In the upper stratosphere, the Andes seem to have greater impact downstream as the emitted westward propagating GWs present across the globe at that latitude (top right plot in Fig. 6).

Such orographic GWs have been seen through other satellite instruments, such as Aura MLS (Wu and Eckermann, 2008) and AMSU-A (Wu et al., 2006). The GW amplitudes in AIRS, however, are the strongest among all even after taking into account the averaging effect. This indicates that mountain waves (MWs) likely possess greater amount of energy toward the high-frequency part of the frequency spectrum (relative to the mean wind), and AIRS is particularly sensitive to them due to its high resolution and the steep viewing angle. In both hemispheres, orographic GW maxima are at high-latitudes (Greenland, Antarctic peninsula) in the lower stratosphere, and the peaks within 50–60 deg become more and more identified in the middle and upper stratosphere (eastern Canada, south tip of Andes). This feature can be attributed to vertical wind structures, as the strong wind near the jet center Doppler-shifts the GWs toward longer vertical wavelength, and GWs near the core of the jet hence have better visibility to AIRS. The orographic GWs are closely associated with the upper level polar night jet, and the location of the enhancements vary from year to year with the shift of the polar night jet. Comparing the 10 hPa map with the 2.5 hPa map, significant increase of GW activities is found in Alaska in January 2005 (Fig. 5) and West of Antarctic Peninsula in July, 2005 (Fig. 6). They are highly variable along the longitudes, and not necessarily related with the jets since they do not locate at the exist region of the jet stream, nor do they show preferred propagation directions. Interestingly, the Brunt-Väisälä frequency (N^2) also peaks at the same locations for these two particular months (not shown). In general, GW amplitudes are much smaller at low altitudes (80 hPa) than at higher levels. At high latitudes the GW activity decreases with altitude independent of longitude and not directly related to the wind velocities. This causes the high-latitude maxima around 10 hPa in Figs. 3 and 4. We will discuss about this feature later on in Sect. 4.3.

In the subtropics and tropics, large GW activities are found in the upper stratosphere over the deep convective regions. The deep convective regions are identified from the ice water content (IWC) from Aura MLS (Wu and Eckermann, 2008). In particular, they are Western Pacific warm pool

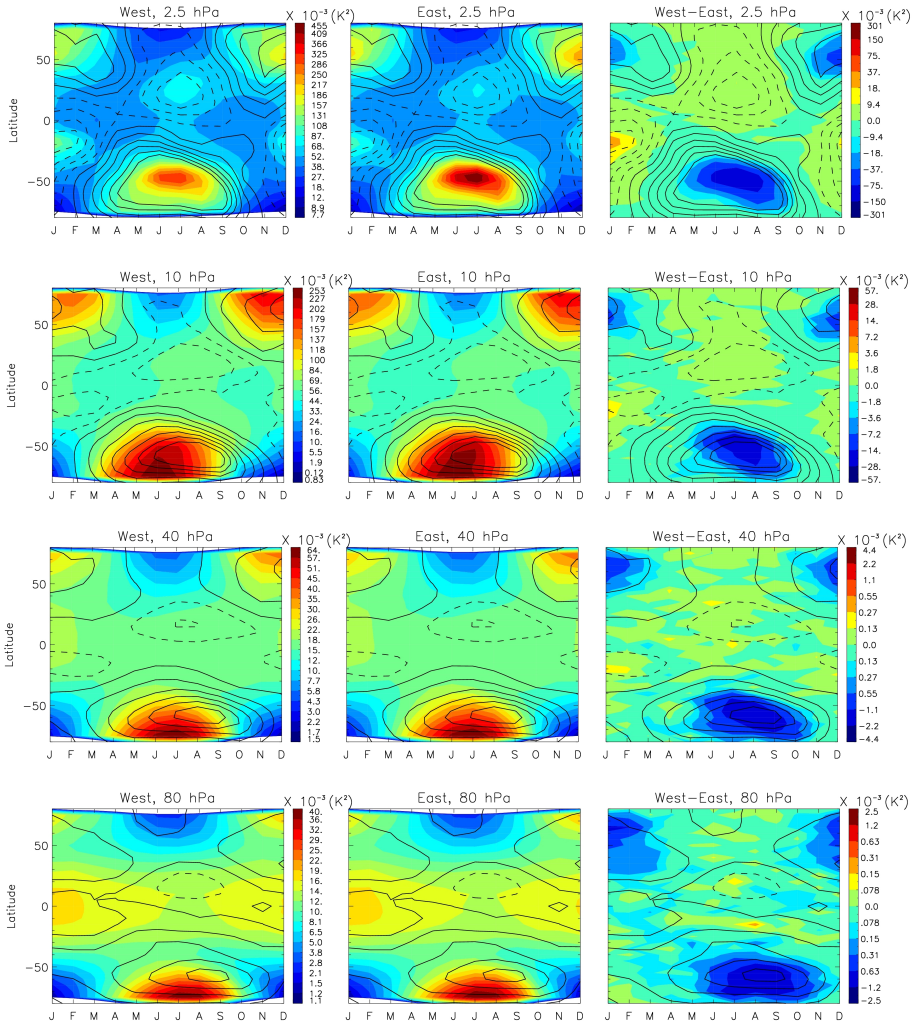

Fig. 7. Multi-year averaged timeseries of zonal mean GW variance for different months at westmost view (first column), eastmost view (second column) and their difference (third column) at 2.5, 10, 40 and 80 hPa from top to bottom. The UK Met Office zonal winds are overplotted in solid (dashed) lines representing westerlies (easterlies) with contour interval of 10 m s^{-1}.

region, Amazon rainforest region, and Central Africa rainforest region for NH winters, and Southeastern US monsoon region and India-South China monsoon region for SH winters. Comparing with Aura MLS, the magnitude of these convectively generated GWs seen from AIRS are smaller. This is consistent with the convective source spectrum suggested by Beres et al. (2004), where source momentum fluxes decrease rapidly at high-frequency part of the spectrum. The AIRS waves tend to propagate eastward relative to the mean wind, but the differences between the two outmost views have values that are marginally above the minimum detectable ones, which means both eastward and westward propagating GWs exist in the upper stratosphere, and the westward propagating ones are smaller than the eastward propagating ones with respect to the integrated magnitude. Convection is known to generate a broad spectrum of GWs that propagate in both directions at top of the deep convection (e.g., Alexander et al., 1997; Beres et al., 2004). Afterwards, the majority of the low-frequency westward propagating GWs are filtered by the easterlies in the tropics and subtropics, but some of the high-frequency waves may survive because they generally have higher phase speeds. These convectively excited high-frequency GWs do not grow into a comparable strength with MWs until they reach the upper stratosphere. In the lower stratosphere, a uniform belt of GW enhancements is found in the tropical region, with some highlights in the deep convective regions, which creates the tropical maximum in the lower stratosphere in the zonal mean maps. This belt has been seen by previous studies using various GW observational instruments (e.g., radiosonde, GPS, IR limb sounders, etc., cf. Preusse et al., 2009). It apparently is not closely associated with the convective sources. It is very interesting that AIRS can see it but AMSU-A, as another nadir viewing sounder, does not see it at all. The belt will be revisited later

on in Sect. 4.3, where we argue that the belt is caused by the propagation of inertia GWs there.

In the high latitude summer hemisphere, GW signals are barely detectable. The 3-pt results without subtracting noise yield a quite uniform distribution of "background-like" variance, which is independent of location and wind. In the NH summer (Fig. 6), it is easy to explain the low wave activity in the NH since the wind at 700 hPa is too weak to generate large orographic GWs (brown hatched regions barely exist in NH in Fig. 6). In the SH summer, we do see some enhancements over the Andes in the lower stratosphere (Fig. 5i), but GWs hardly propagate upward probably because of the critical level filtering effect at the zero-wind line.

Large amplitude MWs vary their location year to year (not shown). The $10\,\mathrm{m\,s^{-1}}$ wind speed at 700 hPa roughly provides a good threshold for generating noticable topographic GWs in the stratosphere. Only at places where westerly wind is consistently strong from low troposphere to upper stratosphere can those GWs grow into significant strengths. Locations of high occurrence of convectively generated GWs are also closely associated with the movement of tropical deep convective zones.

3.3 Temporal variations

A pronounced annual cycle with maximum in the winter hemisphere over mid-high latitudes is found throughout the region of interest in both the variance and difference timeseries. We pick the levels of 2.5, 10, 40 and 80 hPa for the timeseries in Fig. 7, together with the monthly zonal wind derived from UK Met Office dataset. Since the annual cycle is highly repeatable, multi-year AIRS variances are averaged together in Fig. 7 as well as the UKMO winds. The annual cycle found in AIRS are observed, for instance, by Aura-MLS (Wu and Eckermann, 2008), radiosonde (Wang and Geller, 2003), GPS (Tsuda et al., 2000), IR limb sounder (Preusse et al., 2009), etc. Eckermann (1995) attribute the annual cycle in both lidar and rocket sounding observations to seasonal variations in the density stratification of the atmosphere (i.e., N^2). Besides these major factors, source properties can also contribute to the variations in that stronger westerly winds during hemispheric winters tend to create larger MWs, which propagate further downstream under preferable conditions.

The Southern Hemisphere differs from the Northern Hemisphere in terms of the location of the maximum variance. In the Northern Hemisphere, wave variance nearly always peaks at the time when jet is the strongest (December–Feburary), as do the differences. Interestingly, in the Southern Hemisphere, the variance peak occurs ahead of the peak of the westerly jet below 10 hPa, but the difference between the two outmost viewpoints follows the variation of the jet closely, both of which propagate northward in time (May through October). Below 10 hPa, GW amplitudes are largest in July, but the mean wind maximum comes in one month later. A close look at the vertical structure of the zonal wind reveals that tropospheric westerlies in the SH high latitudes actually peak in July (not shown). Another plausible explanation is based on the fact that the coastline of Antarctica is approximately parallel to the latitude lines. Therefore, meridional winds are more important than zonal winds there in generating large amplitude waves. Actually, the meridional wind contours follow the change of GW variance more closely than zonal wind contours (not shown). The Andes seem to be vital at high levels (above 10 hPa) at the intensification stage of the jet speed, while Antarctic Peninsula is more important in lower levels and seems to be a major factor causing the northward movement of the center of polar night jet. This phenomenon is also evident in Fig. 6. Note that the polar night jet in SH winter (e.g., Fig. 3) curves poleward (equatorward) below (above) 10 hPa. Antarctic Peninsula and the Andes perhaps play different roles at different levels in the formation of this shape. In the NH winter, there is no such northward curvature in either the jet center or the center of wave variance maximums. This result again suggests the importance of mountain GWD in shaping and regulating the polar night jets.

Strong interannual variability exists in NH high latitudes (not shown). The polar night jet splits during the winters of 2004, 2006 and 2009 at the polar region, and GW variance reduces a significant amount simultaneously. These are the years of strong sudden stratospheric warming (SSW) events (Lee et al., 2009). Lee et al. (2011) observed enhanced planetary wave activities during the SSW events from Aura MLS observations, and they believe the planetary waves serve as an efficient filter to prevent upward propagation of GWs. More explanations can be found in Dunkerton and Butchart (1984).

The annual cycle also dominates the subtropical stratosphere, but completely opposite phases are found between the upper stratosphere and lower stratosphere. In the upper stratosphere (first row of Fig. 7), GW variance as well as west-east difference peak during hemispheric summers. Zonal mean maps (Figs. 5 and 6) show that the convectively generated GWs grow significantly in the upper stratosphere, which collocate with the easterly jet centers as well. Therefore, this summer peak could be largely explained by the convective source properties. In the lower stratosphere, winter maximum dominates, and this should be again attributed to the variations of density stratification similar to that of the mid-high latitudes (Eckermann, 1995).

The tropical lower stratosphere has an annual cycle with NH winter maximum, and this largely agrees with the fact that deep convections in the SH summers are in general stronger (Liu et al., 2007). QBO signals are relatively weak but still significant compared with the annual cycle, showing very interesting features that will be discussed in the next section. In the middle to upper stratosphere, a prevailing semi-annual cycle is found (not shown), which we believe is a combined effect of background winds (semi-annual

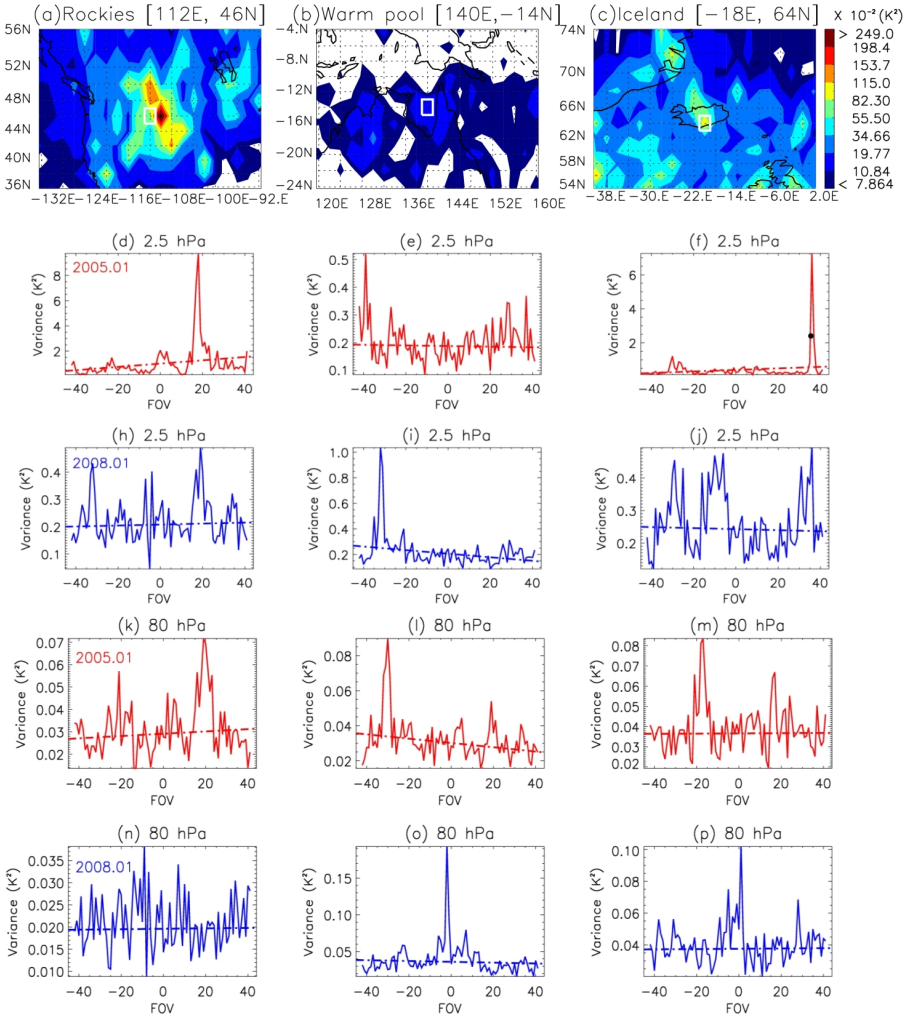

Fig. 8. (a–c) Geographical map of GW variance at eastmost view at three different locations for January 2005 at 2.5 hPa. The GW variances within the white box of **(a–c)** as a function of FOV numbers are plotted in solid for each location at **(d–f)** January 2005, 2.5 hPa; **(h–j)** January 2008, 2.5 hPa; **(k–m)** January 2005, 80 hPa; and **(n–p)** January 2008, 80 hPa. Negative (positive) FOV numbers correspond to west (east) views, and 0 corresponds to nadir view. The linear fits of each FOV curve are overplotted in dash-dotted lines.

oscillations there) and the source (convection crossing the equator twice per year at equinoxes).

4 Discussions

Some new features from AIRS GW observations are worth further discussions. In this section, we will provide in-depth analyses on GW sources, interannual variations, and enhancements from inertia GWs.

4.1 Orographic and convective GW sources

Topographic GWs have been extensively studied during the last decades, and relatively mature parameterization schemes of the mountain GWD have already been employed widely in state-of-art GCMs. These schemes usually take into account factors such as mountain height, surface wind speed, atmospheric stability and the alignment of the mountain ridges (McFarlane, 1987; Bachmeister, 1993). The non-stationary convective GWs received less attention compared to the orographic sources until recent years (Song and Chun, 2005; Beres et al., 2005). As to the parameterization of these GWs, some treat them as “moving mountains”, and some think they create much broader spectra (e.g., Song and Chun, 2005). Both of the orographic and convective GWD parameterizations have free parameters to represent the wave intermittency, which is, by far, the poorest constrained parameter. Other “tunable” parameters include horizontal wavelength, source momentum spectrum, etc. AIRS, as one powerful GW observation instrument, can certainly improve our global understanding on the “observational constraints” of the parameterization schemes. For example, from the

geographical distribution that has been discussed in Sect. 3.2, we can tell that MWs tend to have larger energy variance toward the high-frequency part of the energy spectrum, while it seems to be the other way around for the convective GWs. Besides, some interesting features are found in AIRS, which are quite different from what's been observed before by other instruments.

To look into more details, we pick two orographic GW cases and one convective GW case that are evident in January 2005, which occur at the Rockies, the warmpool region, and Iceland. The monthly mean FOV-dependent GW variance within the white grid box is plotted at 2.5 hPa and 80 hPa for both January 2005 and 2008 in Fig. 8. At first glance, the linear regression line confirms our idea that orographic GWs in general propagate westward while tropical convective GWs propagate eastward, both relatively to the local mean zonal wind. Ideally, if a monochromatic wave exists, we should see a smooth curve with a single peak or no peak depending on whether the upward propagation angle is smaller or larger than 48°. However, multiple peaks stand out in almost all curves in Fig.8d–p, indicating a spectrum of GWs are generated down below. In the lower stratosphere (Fig. 8k–p), convectively excited GWs may have sporadic spikes (Fig. 8i, o) while orographic GWs can generate a rather broad spectrum (Fig. 8n). The peaks of the variance in certain cases are close to the nadir (e.g., Fig. 8o, p), which means those Doppler-shifted GWs propagate almost vertically. By comparing the 2.5 hPa FOV curves with the ones at 80 hPa, we may conclude that background wind plays a leading role in shaping the GW spectrum during the upward propagation. However, three preferred angles at FOV No. 25, No. 0 and No. 20 persist from lower to upper altitudes over the Rockies during January 2005, and the FOV No. 0 and No. 20 also have peaks of GW variance at 2.5 hPa during January 2008, even though no big wave event occurred over the Rockies in January 2008. Similar phenomena happen over Iceland (Fig. 8f,j), and the Andes (not shown). These preferred directions should be associated with the detailed structures of the topography, and background wind is probably another candidate that prefers to select certain angles.

GWs seen by AIRS provide at least two new discoveries about the orographic and convective GWs. For orographic GWs, vertical wavelength is already large at the wave generation level compared with convective GWs, and certain angles are favored for generating large amplitude GWs, which vary among different mountain ranges and vertical wind structures as well. The ratio between peaks and troughs as well as maximum amplitude occurring FOV angles can be used to infer wave intermittency, which is an important wave parameter in GCMs that lacks observational constraints. It is not clear why certain angles are preferred. The reason why large amplitude GWs can be seen in the nadir view is another interesting point and beyond the scope of this study. They remain as potential topics for future investigations.

Convectively generated GWs, as suggested here in AIRS observations, have much smaller wave scales in terms of both vertical and horizontal wavelengths. Therefore, it is expected to have fair amount of momentum flux in the high-frequency end of the momentum spectrum, which also varies quite a lot based on sporadic spikes present in AIRS. The current assumptions of source spectrum (e.g., Song and Chun, 2005; Beres et al., 2004) for convective GWs is, at least, not accurate enough to represent all situations. Note that these curves are all derived from monthly means. Spikes in both mountain and convection cases may simply come from different events, i.e., wave intermittency is a highly variable parameter. More exploration of the details need to be carried out in the future before advice can be given to modelers.

4.2 Interannual variations at the equatorial region

The quasi-biennual oscillation (QBO) wind acts as an efficient GW filter in the tropical lower-middle stratosphere, and the interations between GWs and background winds are, in turn, an essential ingredient in the QBO. Different GWs contribute differently to driving the QBO. Kawatani et al. (2010a, b) were able to simulate a realistic QBO with a high-resolution climate model without parameterizing GWD. Their GCM can resolve part of the inertia GW spectrum (limited by the model's vertical grid resolution), and the simulated QBO has a shorter period than that of the real atmosphere, but with realistic strength and structure. Their work suggests the importance of inertia GWs in generating the QBO. Some other model studies suggest that the momentum deposition associated with the filtered GWs accounts for at least half of the total momentum flux in driving the QBO (Giorgetta et al., 2002; Kawatani et al., 2010a). QBO signals have also been seen in various GW observations, such as radiosonde (Vincent and Alexander, 2000; Wang and Geller, 2003), GPS (Torre et al., 2006), IR limb sounders (Krebsbach and Preusse, 2007) and Aura MLS (Wu and Eckermann, 2008). These instruments are ideal for observing low to middle frequency GWs.

AIRS GWs contain a strong annual cycle in the tropical lower stratosphere (Fig. 7). On top of the annual cycle, a clear QBO signal stands out. After removing the annual cycle, the linear trend, and sub-seasonal oscillations, we present the timeseries of the GW variance/difference anomalies at the equator in Fig. 9. Pronounced GW variance enhancements occur along with the descent of the QBO easterly phase (defined as when the monthly mean zonal wind is easterly, likewise for QBO westerly phase), and a reduction of GW activity happens right before and lasts through the whole period of the descending of the westerly phase (Fig. 9a). Year 2003–2004 is somewhat different from other years, when the enhancement only occurs during the downward propagation period of QBO easterly shear, and a strong negative anomaly occupies the rest of the phase. The GW differences also show preferred zonal propagation directions

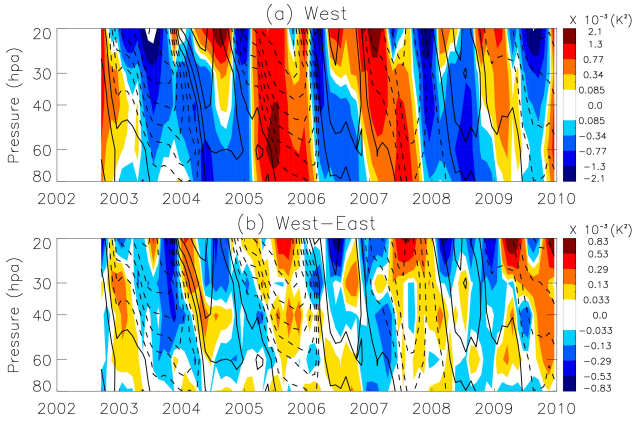

Fig. 9. Monthly mean timeseries (annual cycle and linear trend removed) of the zonally averaged GW variance taken at the westmost view **(a)** and the variance differences between the westmost and the eastmost view **(b)**. The vertical cross-section is taken at the equator from 80 hPa to 20 hPa. 3-month running smooth window is applied to the data to remove the sub-seasonal cycle. UKMO monthly mean zonal winds are overplotted in lines with contour intervals of $5\,\mathrm{m\,s^{-1}}$ and solid (dotted) lines indicating eastward (westward) winds. Variance within $\pm 0.085 \times 10^{-3}\,\mathrm{K}^2$ and difference within $\pm 0.033 \times 10^{-3}\,\mathrm{K}^2$ are uncolored.

during different QBO phases. Although it is more ambiguous in Fig. 9b, in general the GWs that can survive the wind perfer to propagate eastward (westward) in the presence of QBO easterly (westerly) shears. Again, year 2003–2004 is an exception. The other thing to notice is that the QBO can only account for about 1/10 of the variance that can be explained by the annual cycle.

The close correlation shown in Fig. 9 indicates the interactions between QBO winds and some of the AIRS observed GWs. Moreover, it suggests that these GWs may play a more important role for the descent of QBO westerly phase than that of the easterly phase based on the evidence that the suppression (enhancement) of wave activities occurs at the downward propagation of QBO westerly (easterly) shear, i.e., more GWs are removed and hence deposit their momentum fluxes at the downward propagation stage of QBO westerly shear. Deep convection is the most dominant source at the tropics that is responsible for GWs we see in AIRS, as discussed in the last section. Since the upper-troposphere wind is in general easterly, the spectrum of deep-convection generated GWs at the tropopause level inherently has a skewness toward positive phase speed, i.e., eastward propagating GWs dominate. Hence, QBO westerlies tend to filter out more GWs than QBO easterlies, resulting in the observed less GW activity during the QBO westerly phase. This finding is consistent with what has been observed by Aura MLS (Wu and Eckermann, 2006). Some of the previous studies using radiosonde and GPS also found suppression of GWs in the QBO westerly phase (e.g., Sato and Dunkerton, 1997; Wang and Geller, 2003; Torre et al., 2006), but they suggest that this suppression occur right along the descending of the zero-wind line of the QBO westerly phase. This is mainly caused by Kelvin waves that are unavoidably blended in the measurements from radiosonde and GPS. MLS scans along-track (almost meridionally over most of the latitudes), and Kelvin waves are truncated by a technique with short horizontal wavelength cut-off. 7-pt running smooth window we applied on AIRS measurements produces a cut-off wavelength at $\sim$105 km, which can also effectively filter out Kelvin waves. Another possible reason lies in the fact that radiosonde and GPS observes more low-frequency GWs than AIRS does, which are believed to have larger impact on the QBO formation and downward propagation than high-frequency GWs (Kawatani et al., 2010a). Vincent and Alexander (2000) found increased GW activities during QBO easterly phase through radiosonde data over a tropical island, which is a bit different from other radiosonde observations but is consistent with what we observe in AIRS. The reason for the strong negative anomaly during year 2003–2004 remains unclear. It might be associated with other interannual variabilities such as El Nino Sothern Oscillation (ENSO). Due to the limit of AIRS data record length, this conclusion is not definitive, and remain a nice topic for future investigation.

However, the QBO only explains about 10% of the total variability of AIRS GWs, which means AIRS GWs are only slightly modified by the QBO rather than playing a dominant role on the formation/propagation of QBO phases. This is expected as AIRS is mostly sensitive to higher-frequency GWs, which usually propagate into the upper stratosphere and above (Fritts and Alexander, 2003). In fact, the maximum wind speeds of the easterly and westerly associated with the QBO are $-35\,\mathrm{m\,s^{-1}}$ and $20\,\mathrm{m\,s^{-1}}$. At the equator, this converts to a vertical wavelength range of 5.6 to 10 km assuming $N^2 = 5 \times 10^4\,\mathrm{s}^{-2}$. These GWs are too short to be seen by AIRS. Nevertheless, AIRS GWs still contain QBO signals, indicating that AIRS should have some capability of observing relatively short vertical wavelength waves, which will be explained in the next section.

Theoretical work predicts both westward and eastward propagating GWs should both contribute to the QBO formation (Baldwin et al., 2001). This is further confirmed by simulation results from high-resolution GCMs (e.g., Sato et al., 1999; Kawatani et al., 2010a, b). However, it is difficult to separate eastward propagating GWs from massive Kelvin wave signals in radiosonde and GPS observations. The inferred preferred zonal wave propagation direction from AIRS at the equator show both eastward and westward propagation signals with about equal probability to occur (Fig. 9b). The uniqueness of AIRS GW response to QBO winds indicates the power of satellite instruments in obtaining the GW information.

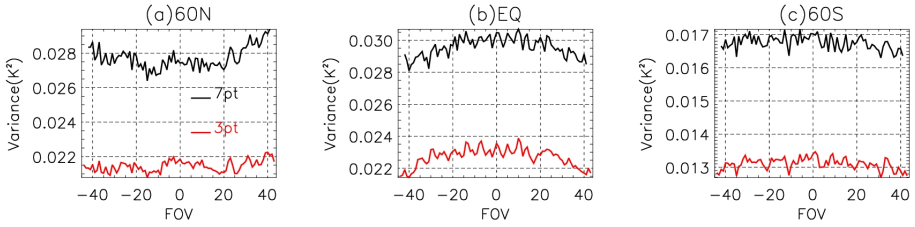

Fig. 10. Zonal mean FOV curves at 80 hPa for 3-pt (red) and 7-pt (black) results at January 2005 at 60° N **(a)**, 0° **(b)** and 60° S **(c)**. The horizontal axes are the number of scanning points along a FOV scan, where −(+)45 corresponds to westmost(eastmost) view, while 0 is at nadir.

4.3 Wave enhancement in the equatorial lower stratosphere and near the winter pole at 10 hPa

MWs are excessively strong in the AIRS observations, which overwhelm other GW signals if we look globally. In the lower stratosphere, however, GWs are stronger in the equatorial region. These GWs are not closely associated with deep convection, as the variance forms a uniform belt (Figs. 5g, h, 6g,h, and bottom row of Fig. 7). By revisiting Fig. 3, we can find that the amplitude of these GWs maximizes at the tropopause (∼ 100 hPa), decreases dramatically right above, and increases again above 80 hPa. These features are in good agreement with previous studies using radiosonde (e.g., Wang and Geller, 2003), GPS (e.g., Ratnam et al., 2004), Aura MLS (Wu and Eckermann, 2008), CRISTA and SABER (Preusse et al., 2006), and high-resolution GCM simulations (e.g., Sato et al., 1999), but are not shown in UARS MLS (Wu and Waters, 1996) nor Aura AMSU-A (Wu, 2004). Meanwhile, there is also a peak at the winter pole at 10 hPa, as shown in Figs. 3 and 4. This is the first observation of such a 10 hPa winter-pole-enhancement. Since this feature is not uniformly distributed among the high-latitude hemisphere winters (Figs. 5 and 6), and the locations vary from year to year (not shown), it is believed not purely caused by underestimation of the instrument noise, but rather a real atmospheric phenomenon.

A careful evaluation of FOV-dependent variance profile ("FOV curve" hereafter) suggests that the 80 and 10 hPa variance enhancements are something other than high-frequency internal GWs and instrumental noise. The zonal mean FOV curves derived at 60° N, 0° and 60° S for January, 2005 at 80 hPa are plotted in Fig. 10. At 60° N, as we would expect to see from topographically generated internal GWs in Northern Hemisphere winter, the variance is the largest at the eastmost view. At 60° S, the FOV curves are basically flat and small, close to the estimated noise level. At the equator, the FOV curve bends downward, with maximum value occurring at the nadir view. This is also true at the two flanks of the polar night jet at middle to upper stratosphere (not shown).

Turbulence can cause "bell" shape FOV curves seen in Fig. 10b due to the fact that the power index for 2-D turbulence is more negative at the off-nadir view than the nadir view and hence the area integral is smaller for the off-nadir view (Gruninger et al., 1998). Since shear instabilities easily occur at the two flanks of the polar night jet, turbulence can be particularly strong there. However, we cannot explain why turbulence is particularly strong in the equatorial lower stratosphere and the winter pole at 10 hPa with this theory. Besides, according to Aumann and Miller (1994), the outmost view has a FOV swath area 4 times larger than that of the nadir view, which would result in a very deeply downward curved FOV-dependent variance profile. Even with noise being already subtracted, the FOV curve in Fig. 10b has a difference between outmost and nadir views of only 7 %, which is way too small to be purely interpreted as the turbulence.

Another explanation of the downward curvature of FOV curves in Fig. 10b invokes short vertical wavelength, long horizontal wavelength, low-frequency inertia GWs. These GWs are probably the cause of the QBO signal presented in the last section. Alexander et al. (2002) proposed the idea that slow GWs have larger probabilities to be observed than fast waves. Since the vertical group velocity is approximately proportional to square of the wave intrinsic frequency, AIRS has a larger chance to observe inertia GWs in the lower stratosphere, and the overall enhancement of wave activity observed in the tropics is largely due to the reason that these inertia GWs propagate slantwise and spread out from the convective source consequently. Since the GW enhancement in the equatorial lower stratosphere observed by AIRS is similar to GWs revealed by radiosonde and GPS as well as simulation results in high-resolution GCMs (e.g., Fig. 8c in Sato et al., 1999), we have more confidence to claim that AIRS observes inertia GW signals.

Here we conduct a simulation to show how AIRS detects inertia GWs of short vertical wavelength in the lower stratosphere. Assuming a constant wave amplitude, only waves with vertical wavelength longer than 12 km are visible in the nadir viewing center tracks. The WF is practically a delta function with respect to long vertical wavelength GWs and therefore yield GW variance at the level where the WF peaks. For waves with vertical wavelength less than 12 km, the convolution of waves of a constant amplitude with AIRS WF will yield a very small variance. If, however, the wave

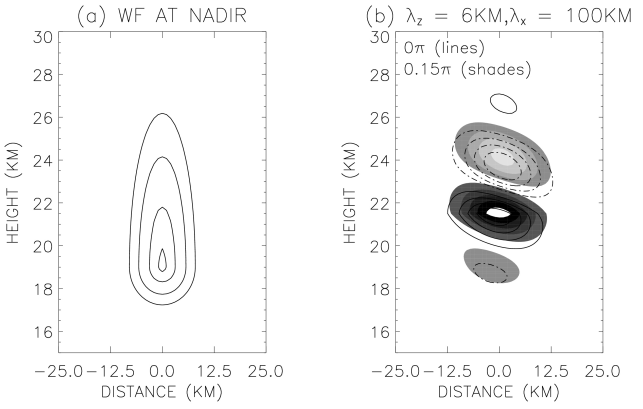

Fig. 11. (a) Weighting function over nadir at 80 hPa as a function of height and along-track distance for the numerical simulation. The contours are 0.5, 0.7, 0.9 and 0.99 of the peak response. The outmost off-nadir weighting function is 4 times broader than that of the nadir. **(b)** One example of the original input wave convolved with the nadir weighting function (lines) and resultant wave with 0.15π phase shift (shades). The wave has horizontal wavelength (λ_x) of 100 km and vertical wavelength (λ_z) of 6 km. Negative values are contoured with dash-dot lines (light colors), and positive values are denoted with solid lines (dark colors). The contour interval is 0.2 of the maximum and minimum amplitudes, respectively.

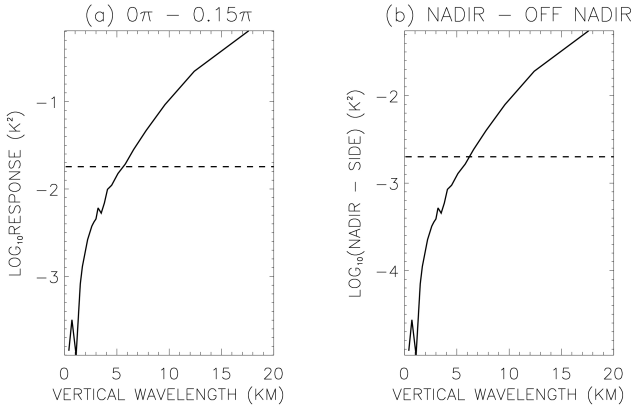

Fig. 12. Variance differences between unshifted wave and the wave shifted by 0.15π for $\lambda_x = 700$ km calculation **(a)**, and the variance difference between nadir FOV and the outmost FOV **(b)** as functions of λ_z. The AIRS observed values (7-pt smoothing window applied) are denoted by dash lines. See text for details.

amplitude varies with height, this can result in an effective narrowing of the weighting function, i.e., the GWs at the edge of the WF cannot be completely cancelled, and will yield some response in AIRS variance. Figure 11a gives an ideal WF at nadir view at 80 hPa to represent mean WFs of multiple AIRS channels we select which all peak at 80 hPa (Appendix A). The WF at the outmost off-nadir view covers an area 4 times broader than that of the nadir WF (see Appendix C for details). Figure 11b shows the GW that is a result of the original imported GW convolved with the WF. The original GW has an amplitude varying with N^2, and the maximum amplitude $A_{\max}$ is 5 K (see Appendix C for details).

The final goal of this experiment is to try to find the best wave parameters that give the convolved variance at the nadir and the variance difference between the nadir and outmost views consistent with the observations (black line in Fig. 10b). In order to compute the variance, we make a horizontal phase shift of $n\pi$ forward of the convolved wave, as shown in shades of Fig. 11b. This procedure is to account for the 7-pt smoothing window we applied to AIRS data. The difference between the two convolved waves are then calculated and compared with the observation (Fig. 10b) at the nadir view. With a fixed λ_x of 700 km, 7-pt smoothing window length (~ 105 km) corresponds to 0.15π phase shift. We can therefore plot out the expected AIRS variance as a function of vertical wavelength λ_z in Fig. 12a. The same procedure can be applied to the outmost off-nadir footprint to obtain a reading of wave variance there, and the difference between the nadir and outmost views can also be computed as shown in Fig. 12b. The two curves meet with the observed values both at $\lambda_z = 6$ km. We tried other λ_x values and it turns out $\lambda_x = 700$ km, $\lambda_z = 6$ km and $A_{\max} = 5$ K gives the best agreements simultaneously. Typical horizontal and vertical wavelengths for equatorial inertia GWs are around 1000 km and 5 km, respectively (Wang and Geller, 2003), and the peak amplitude is around 5 K (Sato et al., 1999), which is in good agreement with our simulation result. The inertia GW variance can also explain why there is no obvious propagation direction in the difference between eastmost and westmost views, as the radiance response involves no propagation direction information whatsoever in this case. The layer near 80 hPa (Fig. 11a) is less affected by the QBO wind than the layers above and hence we still do not see a dominant QBO signal even though these waves are believed to be dominantly inertia GWs. The simulation with a realistic AIRS WF supports the idea that the enhanced GW variance at 10 hPa winter pole is also low-frequency inertia-gravity waves. See Appendix C for details about this experiment.

There are quite a few explanations of why the equatorial maximum weaken rapidly with height. One possible reason is that these inertia GWs with low vertical group velocities simply dissipate. If they speed-up by refraction, the visibility may lessen. Another possibility is that these waves meet the "tropical confinement". Once they propagate off-equator due to the slantwise propagation, they tend to easily meet the lower limit of the frequency, f (inertial frequency), as f increases with latitude (Sato et al., 1999). Hence the tropical belt of GW enhancement disappears at high altitudes (20 hPa and above), and only those high-frequency internal GWs that are closely related with convective sources can survive. Choi et al. (2011) applied 3-D AIRS WFs to their parameterized

convective GWs, and found out that merely any GWs can be seen in the equatorial lower stratosphere since the parameterized GWs are too small in terms of the vertical wavelength and horizontal wavelength as well. Propagating upward, these small GWs are Doppler-shifted toward longer vertical wavelength, and become detectable by AIRS, which agree very well with what we see at middle and upper stratosphere.

A peak at 10 hPa at the winter pole appears in the N^2 field in Fig. C1 of the Appendix C. Therefore, as in the tropical lower stratosphere, inertia GWs should grow again at those levels, but with a short penetration. Convolving with the weighting function, and the GWs result in another enhancement in AIRS variance. Due to the sensitivity limitations, radiosonde and GPS sensors cannot observe those GWs at this level. UARS MLS and Aura AMSU-A cannot see these features probably because of the coarse horizontal resolutions (Wu and Eckermann, 2008). Aura MLS also observes similar equatorial enhancement at lower levels, but not at the 10 hPa winter pole, which remains to be investigated in the future (Wu and Eckermann, 2008).

After all, the AIRS GW variance is believed to be composed of large amplitude internal GWs that are closely related with the local sources (e.g., orography, deep convections), and small amplitude "background-like" inertia GWs that are determined by the shape of the WFs and the shape of the original amplitude spectra. It is shown that AIRS can observe the inertia GWs even though their vertical wavelengths are smaller than AIRS WF thickness. This interpretation might be applicable to explaining signals discovered in other instrument measurements. The two groups of GWs are potentially separable by regressing the variance on N^2. Turbulence is another possibility, but the strength and mechanism remain as a question for future investigation.

5 Conclusions

In this study, climatology of the GW variance and zonal preferred propagation direction measured by Aqua-AIRS are documented. In summary, evidence is found for short horizontal wavelength internal GWs ($\lambda_h \sim 100km$, $\lambda_z > 12km$) forming dedicated geographical maxima that are closely related to localized sources such as topography and deep convection. A generally smaller background of longer horizontal wavelength GWs forms band-like structures for instance in the lower stratosphere tropics. It is remarkable that AIRS can detect these inertia GWs even though their vertical wavelength is smaller than the width of the AIRS weighting function, if the wave amplitude changes notably over the range of detection.

GW induced temperature variance is first succesfully extracted from the brightness temperature variance observed by AIRS by carefully removing instrumental noises at various pressure levels. A total of 50 AIRS channels is used with WFs peaking at various levels covering the entire stratosphere. Because of the nadir viewing geometry and small footprint size, AIRS radiance variance is most sensitive to high-frequency internal GWs with comparable vertical and horizontal wavelengths with wave fronts in parallel to the scanning angle. Large smearing occurs when the wave front is across the AIRS scan, leading to possibility of inferring the preferred GW propagation direction using variance difference between two outmost views.

Comparisons have been carried out throughout the paper between AIRS GW variance and other measurements including satellite and non-satellite instruments (e.g., Aura MLS, Aqua AMSU-A, GPS, radiosonde, GCM simulations, etc.). The GW variance seen by AIRS in general agrees with previous studies in terms of the distributions and variations of maxima. The AIRS GW peaks are generally found to be above high meridionally-oriented mountain ranges, as well as near tropical deep convection regions. Different from others, the GWs observed in AIRS are highly localized, since they are dominated by high-frequency components. This provides better information on GW sources from direct retrievals of GWs, as shown in Alexander and Barnet (2007). The locations of GW peaks vary significantly from year to year. The 700 hPa wind is used to evaluate the GW generation, showing that stratospheric GWs tend to grow into great amplitudes at the places with wind speed greater than $10\,\mathrm{m\,s^{-1}}$ collocated with the upper-level jet maxima. In the tropics, the deep convection controls the GW variance peaks.

The inferred preferred zonal propagation directions of GWs seen in AIRS are opposite to the mean zonal wind directions. Topographic GWs in the winter high-latitudes tend to propagate westward relative to the mean flow, while convectively excited GWs in the tropics and subtropics tend to propagate eastward relative to the mean winds. The preferred wave propagation becomes clearer with increasing altitude, suggesting effective wave filtering and increasing GWD on the mean flow. The GW variance contours do not exactly follow the wind contours, suggesting less filtering of the high-frequency GWs, which propagate through and become more important in the mesosphere and above.

An analogous approach of determining wave propagation direction has also been carried out on Aura MLS observations (Wu and Eckermann, 2008), where wave preferred meridional propagation direction is inferred in a similar way considering the fact that MLS scans along the orbit. One can therefore obtain a more complete picture of the GW horizontal propagation direction from the combined AIRS and MLS results. Recent studies show that convective GWD parameterizations are sensitive to the wave propagation direction, which is set to be a free parameter in the model (Song and Chun, 2005, 2008). Observations of the propagation direction by AIRS may help to constrain this parameter.

The new findings with AIRS GW variance differ from other GW observations in three aspects:

Table A1. Comparison of sensitivity to GW parameters from various satellite measurement techniques. Spectral coverage and sensitivity peaks depend on the techniques that are used in the corresponding reference.

Instrument Name	Altitude Range	Spectral coverage	Peak Sensitivity	Reference
AIRS	surface −40 km	$\lambda_z > 12$ km, $\lambda_h > 13$ km	$\lambda_z = \lambda_h \sim 100$ km	this paper
GPS	10–30 km	$\lambda_h > 100$ km	$\lambda_h/\lambda_z \gg 10$	Alexander et al. (2008)
Aura-MLS	15–50 km	$\lambda_z > 5$ km, $\lambda_h > 50$ km	$\lambda_z = 10$ km, $\lambda_h = 100$ km	Wu and Eckermann (2008)
CRISTA	15–60 km	$\lambda_z > 5$ km, $\lambda_h > 100$ km	$\lambda_h/\lambda_z = 100$	Preusse et al. (2009)

Firstly, AIRS 90-footprint FOV-depedent GW variance above mountain ranges and deep convection occurs with preferred angles. Because of the AIRS steep viewing angle, this finding indicates that really high-frequency GWs with large amplitudes are present, and mainly excited from orographic and convective sources. It requires further investigation on why certain angles are preferred, which is potentially a parameter missing or poorly constrained (e.g., wave intermittency) in all GWD parameterization schemes.

Secondly, the QBO signals observed in AIRS are different from other measurements that mainly observe inertia GWs and Kelvin waves. With relatively fast vertical group velocity, these high-frequency internal GWs seen in AIRS are more difficult to be filtered out by QBO winds, and hence they are less important in the formation and descending of QBO phases. AIRS GWs that are affected by QBO might be low-frequency inertia GWs that directly cause the lower stratosphere maxima of wave intensity. The QBO has not been well simulated so far in GCMs. On one hand, the coarse vertical resolution results in deficiency in resolving some inertia GWs. On the other hand, the poorly observationally constrained GWD parameterization schemes cannot precisely represent the characteristics of high-frequency GWs. AIRS not only provides abundant information on the latter on to improve our understanding of high-frequency GWs, but also show potential to observe low-frequency inertia GWs.

Lastly, the most important and encouraging finding from this work the AIRS capability of detecting short vertical wavelength inertia GWs, by assuming inertia GWs' amplitudes varying only with background stabilities. AIRS appears to be highly selective on high-frequency GWs, and therefore we literally can separate the GW variance between the inertia-gravity and high-frequency components. Moreover, this new capability will help us to further understand GW characteristics as observed by other sensors.

This paper provides the first climatological report of GW characteristics from nadir viewing sounders. Since AIRS is sensitive to high-frequency GWs, the results from this study also provide the first global survey of the characteristics and properties of high-frequency GWs. Some large-amplitude GW events as well as FOV-dependent variance can be studied in further detail with models. Improving the GWD parameterizations with the AIRS GW observations is another important task to explore in future study.

Appendix A

Channel numbers and the estimated noise level

The channel numbers we used in this paper are listed below in Table A2. Together we also give the estimated noise from "3-pt running average window" method and the provided instrument NEdT on 30 August 2002. The minimum detectable GW variances for zonal means and monthly maps are listed in the last two columns. Bold numbers in the 2nd column are channels that locate at the wings of the radiance spectrum and have no paired channels. These channels are particularly sensitive to small drift in the wavelength while others are stable.

Appendix B

3-pt analyses result

As mentioned in the main text, 7-pt is the best filter size among the ones we have tested (3-pt, 7-pt and 15-pt). To better illustrate this point, 3-pt analysis results are shown in Fig. B1 and Fig. B2 (January and July of 2005, respectively). The overall structure is nearly identical to 7-pt results, but the amplitude is in general smaller than that of 7-pt analysis. We hence can conclude that the signals are robust, and GWs captured by 7-pt filter have larger power on the spectrum than those from 3-pt filter.

Appendix C

Some details about the simulation

In the simulation mentioned in Sect. 4.3, we assume the imported wave amplitude varies with N. The reason is as follows. Eckermann (1995) derived temperature variance as:

$$\overline{\hat{T'^2}} = \frac{N^2}{g^2}\left[1-(f/\omega)^2\right]\left(\overline{u'^2}+\overline{v'^2}\right) \quad \text{(C1)}$$

where g, u', and v' are the gravitional acceleration, zonal wind perturbation, and meridional wind perturbation caused by GWs, respectively. $\overline{\hat{T'^2}} = \overline{T'^2}/T_0^2$, where T' is the

Table A2. A list of channel numbers, noise, NEdT, and minimum detectable GW variance at each pressure level. Bold numbers in the 2nd column are channels that are unpaired. See context for details.

Pressure (hPa)	Channel numbers	Noise (K^2)	NEdT (K^2)	Min. detectable GW var. ($\times 10^{-3}$ K^2) Zonal mean	Map
2	74	0.149	0.165	3.78	26.64
2.5	75	0.147	0.166	3.72	26.22
3	76	0.143	0.161	3.63	25.55
4	77	0.145	0.160	3.66	25.80
7	**78**	0.153	0.162	3.88	27.34
10	**79**	0.182	0.172	4.62	32.53
20	81, 82	0.084	0.078	2.14	15.05
30	**102**, **108**, **114**, **120**, 125, 126	0.039	0.029	0.98	6.88
40	64, 88, 90, **94**, **100**, 106, 118	0.033	0.028	0.83	5.86
60	66, 68, 70, 86, 87, 91, 93, **97**, 130	0.026	0.018	0.66	4.68
80	92, 98, 104, 105, 110, 111, **116**, 117, 122, 123, 128, 129, 134, 140	0.020	0.011	0.50	3.54
100	132, 133, 138, 139, 149, 152	0.026	0.014	0.67	4.73

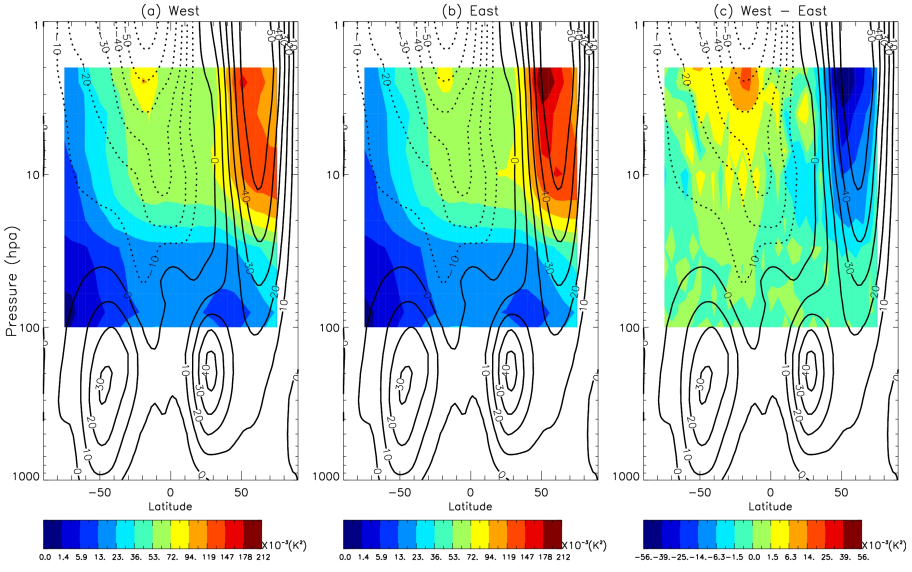

Fig. B1. Same with Fig. 3, but 3-pt filter is applied instead of 7-pt filter.

absolute temperature perturbation, while T_0 is the background temperature. The overbars denote the column average.

Think of it physically. Larger N^2 corresponds to more stable atmosphere, which means the potential temperature increases more rapidly with height. Therefore, same oscillations in height would cause larger temperature perturbations. By assuming that waves neither break nor meet saturations, the vertical group velocity varies inversely with N^2, so that the wave activity coming up from below accumulates in the lowermost tropical stratosphere even if the waves are initially conservative there.

The zonal mean values of N^2 at January, 2005 are shown in Fig. C1. The input 2-D wave amplitude A is assumed to be proportional to N at the equator, which is approximated as:

$$A(x,z) = \begin{cases} A_0 \cos(\frac{2\pi z}{\lambda_z} + \frac{2\pi x}{\lambda_x}) e^{\frac{-(z-z_{60})}{\lambda_z}}, & \text{if } z \geq z_{60} \\ A_0 \cos(\frac{2\pi z}{\lambda_z} + \frac{2\pi x}{\lambda_x}) e^{\frac{-|z-z_{60}|}{4\lambda_z}}, & \text{if } z < z_{60} \end{cases} \quad \text{(C2)}$$

where $z_{60} \sim 21.5$ km roughly corresponds to the geometry height at 60 hPa. x is the along-track distance, and z is the height.

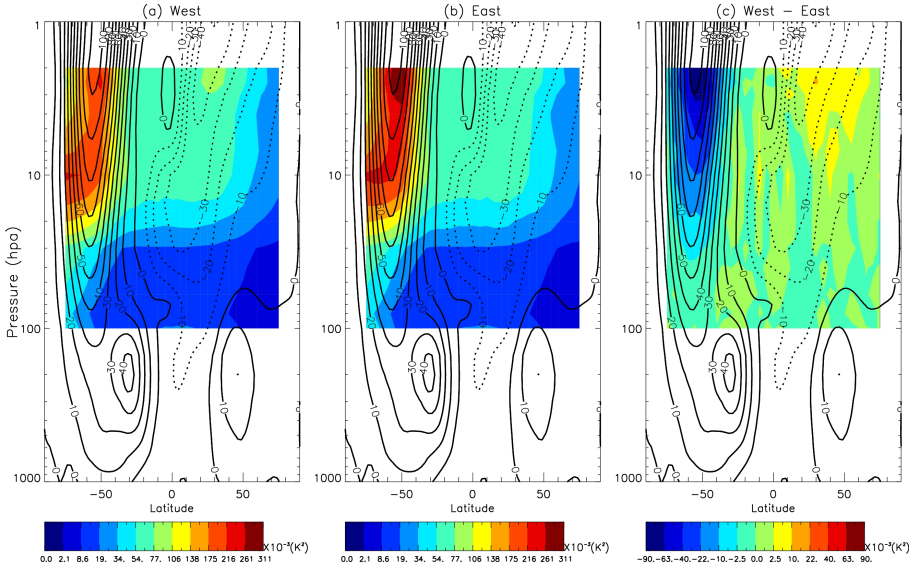

Fig. B2. Same with Fig. B1, except for 2005.07.

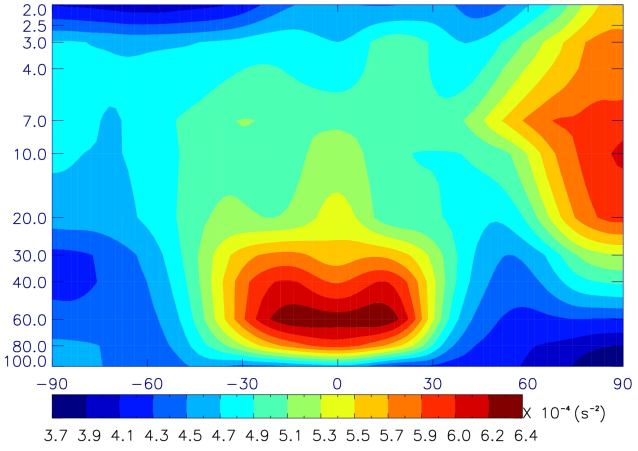

Fig. C1. Zonal mean of the Brunt-Väisälä frequency (N^2) as a function of latitude and height for January 2005, derived from ERA Interim dataset.

The weighting function $WF(x,y,z)$ for AIRS can be calculated directly from radiative transfer models (e.g., Eckermann et al., 2007). Here we use a 2-D function combined with two Gaussian type functions to approximate the actual weighting function. $wf(x,z)$ at the nadir at 80 hPa is defined as:

$$wf(x,z) = \begin{cases} e^{\left(\frac{-(z-z_{80})}{\sqrt{2}\times 6.1}\right)^2} e^{\left(\frac{x}{\sqrt{2}\times 6.75}\right)^2}, & \text{if } z \geq z_{80} \\ e^{\left(\frac{-(z-z_{80})}{\sqrt{2}\times 1.5}\right)^2} e^{\left(\frac{x}{\sqrt{2}\times 6.75}\right)^2}, & \text{if } z < z_{80} \end{cases} \quad \text{(C3)}$$

and

$$WF(x,z) = \frac{wf(x,z)}{\iint wf(x,z)\mathrm{d}x\mathrm{d}z} \quad \text{(C4)}$$

An example of this weighting function has been included in Fig. 11a. At the outmost off-nadir view, the width of this weighting function on along-track direction is broadened by a factor of 5.

Acknowledgements. This work is performed at Jet Propulsion Laboratory, California Institute of Technology, under contract with NASA. The authors acknowldge the supports from NASA Earth Sciences program and Naval Research Laboratory 6.1 research program. J. Gong is greatful to Moustafa Chahine, Kaoru Sato, Hye-Young Chun, and Stephen Licata for helpful discussions and comments. Two reviewers and editor's comments are highly appreciated.

Edited by: T. J. Dunkerton

References

Alexander, M. J. and Barnet, C.: Using satellite observations to constrain parameterizations of gravity wave effects for global models, J. Atmos. Sci., 64, 1652–1665, 2007.

Alexander, M. J. and Holton, J. R.: A model study of zonal forcing in the equatorial stratosphere by convectively induced gravity waves, J. Atmos. Sci., 54, 408–419, 1997.

Alexander, M. J. and Rosenlof, K. H.: Gravity wave forcing in the stratosphere: observational constraints from the upper atmosphere research satellite and implications for parameterization in global models, J. Geophys. Res., 108, 4597–4611, 2003.

Alexander, M. J., Tsuda, T., and Vincent, R. A.: On the latitudinal variations observed in gravity waves with short vertical wavelengths, J. Atmos. Sci., 59, 1394–1404, 2002.

Alexander, M. J., Tsuda, T., and Vincent, R.: On the latitudinal variations observed in gravity waves with short vertical wavelengths, J. Atmos. Sci., 59, 1652–1665, 2002.

Alexander, M. J., Geller, M., McLandress, C., Polavarapu, S., Preusse, P., Sassi, F., Sato, K., Eckermann, S., Ern, M., Hertzog, A., Kawatani, Y., Pulido, M., Shaw, T. A., Sigmond, M., Vincent, R., and Watanabe, S.: Recent developments in gravity-wave effects in climate models and the global distribution of gravity-wave momentum flux from observations and models, Q. J. Roy. Meteor. Soc., 136, 1103–1124, 2010.

Alexander, S. P., Tsuda, T., Kawatani, Y., and Takahashi, M.: Global distribution of atmospheric waves in the equatorial upper troposphere and lower stratosphere: COSMIC observations of wave mean flow interactions, J. Geophys. Res., 113, D24115, doi:10.1029/2008JD010039, 2008.

Aumann, H. H. and Miller, C.: Atmospheric infrared sounder (AIRS) on the Earth observing system, Opt. Engin., 33, 776–784, 1994.

Bacmeister, J. T.: Mountain-wave drag in the stratosphere and mesosphere inferred from observed winds and a simple mountain-wave parameterization scheme, J. Atmos. Sci., 50, 377–399, 1993.

Baldwin, M. P., Gray, L. J., Dunkerton, T. J., Hamilton, K., Haynes, P. H., Randel, W. J., Holton, J. R., Alexander, M. J., Hirota, I., Horinouchi, T., Jones, D. B. A., Kinnersley, J. S., Marquardt, C., Sato, K., and Takahashi, M.,: The quasi-biennial oscillation, Rev. Geophys., 39, 179–229, 2001.

Beres, J. H., Alexander, M. J., and Holton, J. R.: A method of specifying the gravity wave spectrum above convection based on latent heating properties and background wind, J. Atmos. Sci., 61, 324–337, 2004.

Beres, J. H., Garcia, R. R., Boville, B. A., and Sassi, F.: Implementation of a gravity wave source spectrum parameterization dependent on the properties of convection in the Whole Atmosphere Community Climate Model (WACCM), J. Geophys. Res., 110, D10108, doi:10.1029/2004JD005504, 2005.

Choi, H.-J., Chun, H.-Y., Gong, J., and Wu, D. L.: Comparison of gravity wave temperature variances between the ray-based parameterization of convective gravity waves and AIRS observations, J. Geophys. Res., doi:10.1029/2011JD016900, 2012.

Dunkerton, T. J.: Inertia-Gravity waves in the stratosphere, J. Atmos. Sci., 41, 3396–3404, 1984.

Dunkerton, T. J. and Butchart, N.: Propagation and selective transmission of internal gravity waves in a sudden warming, J. Atmos. Sci., 41, 1443–1460, 1984.

Eckermann, S. D.: On the observed morphology of gravity-wave and equatorial-wave variance in the stratosphere, J. Atmos. Terr. Phys., 57, 105–134, 1995.

Eckermann, S. D., Ma, J., Wu, D. L., and Broutman, D.: A three-dimensional mountain wave imaged in satellite radiance throughout the stratosphere: evidence of the effects of directional wind shear, Q. J. Roy. Meteor. Soc., 133, 1959–1975, 2007.

Fritts, D. C. and Alexander, M. J: Gravity wave dynamics and effects in the middle atmosphere, Rev. Geophys., 41, 1003, doi:10.1029/2001RG000106, 2003.

Giorgetta, M. A., Manzini, E., and Roeckner, E.: Forcing of the quasi-biennial oscillation from a broad spectrum of atmospheric waves, Geophys. Res. Lett., 29, 1245, doi:10.1029/2002GL014756, 2002.

Gruninger, J., Duff, J. W., Brown, J. H., and Blumberg, W. A. M.: Radiation transport effects and the interpretation of infrared images of gravity waves and turbulence, P. Soc. Photo-Opt. Ins., 3495, 122–135, 1998.

Hamill, P. and Toon, O. B.: Polar stratospheric clouds and the ozone hole, Phys. Today, 44, 34–42, 1991.

Kawatani, Y., Watanabe, S., Sato, K., Dunkerton, T. J., Miyahara, S., and Takahashi, M.: The roles of equatorial trapped waves and internal inertia-gravity waves in driving the quasi-biennial oscillation. Part I: zonal mean wave forcing, J. Atmos. Sci., 67, 963–980, 2010a.

Kawatani, Y., Watanabe, S., Sato, K., Dunkerton, T. J., Miyahara, S., and Takahashi, M.: The roles of equatorial trapped waves and internal inertia-gravity waves in driving the quasi-biennial oscillation. Part II: three-dimensional distribution of wave forcing, J. Atmos. Sci., 67, 963–980, 2010b.

Kim, Y.-J., Eckermann, S. D., and Chun, H.-Y.: An overview of the past, present and future of gravity-wave drag parametrization for numerical climate and weather prediction models, Atmos. Ocean., 41, doi:10.3137/ao.410105, 2003.

Krebsbach, M., and P. Preusse: Spectral analysis of gravity wave activity in SABER temperature data, Geophys. Res. Lett., 34, L03814, doi:10.1029/2006GL028040, 2007.

Lane, T. P. and Moncrieff, M. W.: Characterization of momentum transport associated with organized moist convection and gravity waves, J. Atmos. Sci., 67, 3208–3225, 2010.

Lee, J. N., Wu, D. L., Manney, G. L., and Schwartz, M. J.: Aura Microwave Limb Sounder observations of the northern annular mode: from the mesosphere to the upper troposphere, Geophys. Res. Lett., 36, L20807, doi:10.1029/2009GL040678, 2009.

Lee, J. N., Wu, D. L., Manney, G. L., Schwartz, M. J., Lambert, A., Livesey, N. J., Minschwaner, K. R., Pumphrey, H. C., and Read, W.G.: Aura Microwave Limb Sounder observations of the polar middle atmosphere: dynamics and transport of CO and H_2O, J. Geophys. Res., 116, D05110, doi:10.1029/2010JD014608, 2011.

Liu, C. T., Zipser, E. J., and Nesbitt, S. W.: Global distribution of tropical deep convection: differet perspectives from TRMM infrared and radar data, J. Climate, 20, 489–503, 2007.

McFarlane, N. A.: The effect of orographically excited gravity wave drag on the general circulation of the lower stratosphere and troposphere, J. Atmos. Sci., 44, 1775–1800, 1987.

McLandress, C., Alexander, M. J., and Wu, D. L.: Microwave Limb Sounder observations of gravity waves in the stratosphere: a climatology and interpretation, J. Geophys. Res., 105, 11947–11967, 2000.

Preusse, P., Eckermann, S. D., Ern, M., Oberheide, J., Picard, R. H., Roble, R. G., Riese, M., Russell, J. M., and Mlynczak, M. G.: Global ray tracing simulations of the SABER gravity wave climatology, J. Geophys. Res., 114, doi:10.1029/2008JD011214, 2009.

Ratnam, M. V., Tetzlaff, G., and Jacobi, C.: Global and seasonal variations of stratospheric gravity wave activity deduced from the CHAMP/GPS Satellite, J. Atmos. Sci., 61, 1610–1620, 2004.

Richter, Jadwiga H., Fabrizio Sassi, Rolando R. Garcia: Toward a Physically Based Gravity Wave Source Parameterization in a General Circulation Model, J. Atmos. Sci., 67, 136–156, 2010.

Sato, K. and Dunkerton, T. J.: Estimates of momentum flux associated with equatorial Kelvin and gravity waves, J. Geophys. Res., 102, 26247–26261, doi:10.1029/96JD02514, 1997.

Sato, K., O'Sullivan, D. J., and Dunkerton, T. J.: Low-frequency inertia-gravity waves in the stratosphere revealed by three-week

continuous observation with the MU radar, Geophys. Res. Lett., 24, 1739–1742, doi:10.1029/97GL01759, 1997.

Sato, K., Kumakura, T., and Takahashi, M.: Gravity waves appearing in a high-resolution GCM simulation, J. Atmos. Sci., 56, 1005–1018, 1999.

Scaife, A. A., Butchart, N., and Warner, C. D.: Impact of a spectral gravity wave parameterization on the stratosphere in the Met Office unified model, J. Atmos. Sci., 59, 1473–1489, 2002.

Song, I.-S. and Chun, H.-Y.: Momentum flux of convectively forced internal gravity waves and its application to gravity wave drag parameterization. Part I: theory, J. Atmos. Sci., 62, 136–156, 2005.

Song, I.-S. and Chun, H.-Y.: A lagrangian spectral parameterization of gravity wave drag induced by cumulus convection, J. Atmos. Sci., 65, 1204–1224, 2008.

De la Torre, A., Schmidt, T., and Wickert, J.: A global analysis of wave potential energy in the lower stratosphere derived from 5 years of GPS radio occultation data with CHAMP, Geophys. Res. Lett., 33, L24809, doi:10.1029/2006GL027696, 2006.

Vincent, R. A. and Alexander, M. J.: Gravity waves in the tropical lower stratosphere: an observational study of seasonal and interannual variability, J. Geophys. Res., 105, 17971–17982, 2000.

Wang, B. and Rui, H.: Synoptic climatology of transient tropical intraseasonal convection anomalies: 1975–1985, Meteorol. Atmos. Phys., 44, 43–61, 1990.

Wang, L. and Geller, M. A.: Morphology of gravity-wave energy as observed from 4 years (1998–2001) of high vertical resolution U.S. radiosonde data, J. Geophys. Res., 108, doi:10.1029/2002JD002786, 2003.

Wheeler, M., Kiladis, G. N., and Webster, P. J.: Large-scale dynamical fields associated with convectively coupled equatorial waves, J. Atmos. Sci., 57, 613–640, 2000.

Wu, D. L.: Mesoscale gravity wave variances from AMSU-A radiances, Geophys. Res. Lett., 31, L12114, doi:10.1029/2004GL019562, 2004.

Wu, D. L. and Eckermann, S. D.: Global gravity wave variances from Aura MLS: characteristics and interpretation, J. Atmos. Sci., 65, 3695–3718, 2008.

Wu, D. L. and Waters, J. W.: Gravity-wave-scale temperature fluctuations seen by the UARS MLS, Geophys. Res. Lett., 23, 3289–3292, 1996.

Wu, D. L., Preusse, P., Eckermann, S. D., Jiang, J. H., Juarez, M. T., Coy, L., and Wang, D. Y.: Remote sounding of atmospheric gravity waves with satellite limb and nadir techniques, Adv. Space Res., 37, 2269–2277, 2006.